Emergence of criticality through a cascade of delocalization transitions in quasiperiodic chains

V. Goblot [1,5], A. Štrkalj [2,5], N. Pernet[1], J. L. Lado [2,3], C. Dorow[1], A. Lemaître [1], L. Le Gratiet[1], A. Harouri[1], I. Sagnes [1], S. Ravets [1], A. Amo [4], J. Bloch[1✉] and O. Zilberberg [2✉]

Conduction through materials crucially depends on how ordered the materials are. Periodically ordered systems exhibit extended Bloch waves that generate metallic bands, whereas disorder is known to limit conduction and localize the motion of particles in a medium[1,2]. In this context, quasiperiodic systems, which are neither periodic nor disordered, demonstrate exotic conduction properties, self-similar wavefunctions and critical phenomena[3]. Here, we explore the localization properties of waves in a novel family of quasiperiodic chains obtained when continuously interpolating between two paradigmatic limits[4]: the Aubry–André model[5,6], famous for its metal-to-insulator transition, and the Fibonacci chain[7,8], known for its critical nature. We discover that the Aubry–André model evolves into criticality through a cascade of band-selective localization/delocalization transitions that iteratively shape the self-similar critical wavefunctions of the Fibonacci chain. Using experiments on cavity-polariton devices, we observe the first transition and reveal the microscopic origin of the cascade. Our findings offer (1) a unique new insight into understanding the criticality of quasiperiodic chains, (2) a controllable knob by which to engineer band-selective pass filters and (3) a versatile experimental platform with which to further study the interplay of many-body interactions and dissipation in a wide range of quasiperiodic models.

Coherent localization of waves is one of the most fundamental effects affecting the conduction properties of materials[2]. In pristine periodic mediums, wave-like excitations are expected to propagate ballistically, following their specific wave equation. Commonly, the presence of disorder reduces the wave propagation, possibly driving it to a diffusive instead of a ballistic regime. With increasing disorder in a system, a metal-to-insulator transition occurs and the waves localize. This is known as Anderson's localization transition[1,2,9]. Such disorder effects are found in a variety of physical systems[10,11].

Wave propagation in quasiperiodic media is more complex[3]. These systems are ordered but non-periodic, and thus fall between periodic and randomly disordered systems. The physics of quasiperiodic systems is known to show unconventional phenomena such as a one-dimensional (1D) localization transition at a finite (quasi-) disorder strength[5,6,12], fractal eigenmodes[7,8] and critical behaviour[3,6]. Among the variety of quasiperiodic models, two canonical examples are the Aubry–André (AA)[5,6] and Fibonacci models[7,8], which are currently drawing much attention, in particular, in the context of many-body localization[13–17]. The quasiperiodicity of the AA model enters in the form of an on-site cosine modulation incommensurate with the underlying periodic lattice spacing, whereas the Fibonacci

model has a modulation with two discrete values that appear interchangeably according to the Fibonacci sequence. Interestingly, the AA and Fibonacci modulations have very different localization properties. Specifically, the AA model shows a unique self-dual localization transition[5,6], whereas the Fibonacci model always has critical wavefunctions[7,8]. Recently, it has been shown that these two paradigmatic models belong to the same topological class and can be viewed as two limits of an interpolating Aubry–André–Fibonacci (IAAF) model[4,18,19]. The IAAF model has been useful for the description of the topological properties of Fibonacci chains[4,18,20] and for generating topological pumps[19,21]. The IAAF model also provides a unique playground to explore how criticality develops during a smooth interpolation between the AA and Fibonacci models.

In this work, we investigate, both theoretically and experimentally, the localization phase diagram of the IAAF model. We show that, along the continuous deformation of the AA into a Fibonacci model, eigenmodes undergo a cascade of band-selective localization/delocalization transitions. We report an experimental observation of one of these transitions using polaritonic 1D wires, which are particularly suitable for direct imaging of the modes both in real and reciprocal space in complex potential landscapes. With our combined theoretical and experimental analysis, we identify the mechanism behind the cascade of localization/delocalization transitions, which involves hybridization of localized modes that thus gradually extend to become critical in the limit of the Fibonacci model. Interestingly, the cascade to criticality appears in quantized plateaux that gradually increase the eigenmode localization length.

The IAAF model[4,18,19] is a 1D tight-binding chain with a quasiperiodic on-site potential modulation

$$H\psi_j = t(\psi_{j+1} + \psi_{j-1}) + \lambda V_j(\beta)\psi_j \qquad (1)$$

where ψ_j is the wavefunction at site j, t is the nearest-neighbour hopping amplitude and λ is the amplitude of the on-site potential modulation. The on-site potential (Fig. 1a) is defined as

$$V_j(\beta) = -\frac{\tanh[\beta(\cos(2\pi bj + \phi) - \cos(\pi b))]}{\tanh\beta} \qquad (2)$$

with the spatial modulation frequency taken as the inverse of the golden mean, $b = 2/(\sqrt{5} + 1)$. In Fig. 1a, we show that the continuous function, out of which the discrete values of $V_j(\beta)$ are sampled, becomes steeper with increasing β. As a result, the range of possible values for V_j shrinks and converges to the two values of the Fibonacci limit. Because the frequency b is irrational, the potential
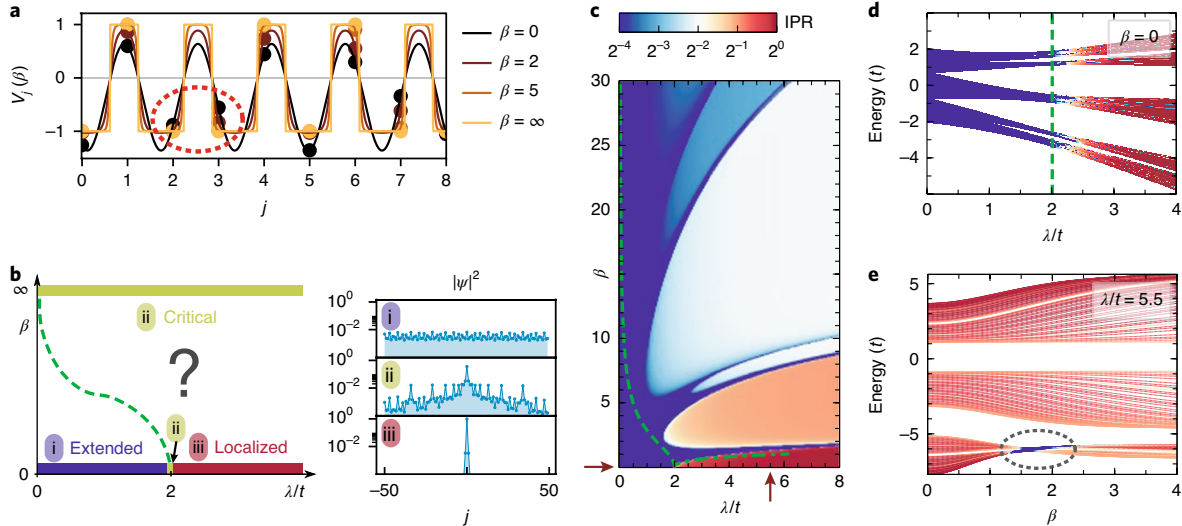
Fig. 1 | IAAF modulation and theoretical localization phase diagram. a, Evaluation of the spatial on-site potential (equation (2)) for several values of β. The two limiting cases are the AA modulation for $\beta = 0$ (black line) and the Fibonacci modulation for $\beta = \infty$ (orange line). The pair of states circled in red are nearest neighbours in space and are close in energy such that they hybridize with a finite hopping strength. **b**, Left: localization phase diagram explored in this Letter. At $\beta = 0$, the AA localization transition occurs at $\lambda/t = 2$, while for $\beta = \infty$ the eigenmodes are always critical. The dashed green line (also shown in **c**) marks the decrease in the extended region obtained using a generalized self-duality argument (Supplementary Section I). Right: typical spatial distribution for extended (i), critical (ii) and localized (iii) modes. **c**, Inverse participation ratio (IPR) (equation (3)) of the lowest eigenmode of the tight-binding model (equation (1)) as a function of β and λ. Red arrows mark β and λ values corresponding to **d** and **e**, respectively. The dash-dotted green line marks the analytically obtained transition line for the lowest-energy state (Supplementary Section II). **d**, The IPR of all eigenmodes of equation (1) as a function of energy and λ/t for $\beta = 0$ (that is, in the AA limit). The dashed green line marks the critical point at $\lambda/t = 2$. **e**, The IPR of all eigenmodes of equation (1) as a function of energy and β for $\lambda/t = 5.5$. At $\beta \approx 1.5$, the lowest-energy set of eigenmodes become extended (dashed oval). In **c–e** we evaluated the IPR on a chain with $L = 610$ sites.

is incommensurate with the underlying lattice and the model is quasiperiodic. Parameter ϕ acts as a global spatial shift of the potential and, although crucial for many effects, such as topological pumping[19–21], it does not affect the localization properties. The tunable parameter β provides a knob by which to interpolate between two known limiting cases: (1) $\beta \to 0$ reduces to the AA modulation[5,22], up to a constant energy shift $V_j^{AA}(\beta) = \cos(2\pi bj + \phi) - \cos(\pi b)$; (2) $\beta \to \infty$ corresponds to a step potential switching between ± 1 values according to the Fibonacci sequence[7,8].

Unlike Anderson localization under on-site disorder[1], the localization transition for the AA model ($\beta = 0$) occurs for all eigenmodes at the same non-zero critical point[5,6] (see x axis of Fig. 1b). The critical point can be obtained using a self-duality argument[5,6]: for $\lambda/t < 2$, all modes are extended, for $\lambda/t > 2$ they are localized, and at the critical point $\lambda/t = 2$, all the modes are critical and self-similar with a power-law spatial decay (Fig. 1b). In the limit of $\beta \to \infty$, all the eigenmodes of the Fibonacci model are critical for any finite $\lambda/t > 0$ (refs. [7,8]). The main goal of this work is to explore the IAAF localization phase diagram and understand how AA modes continuously develop into critical Fibonacci modes. Note that previous studies of deformations of a cosine potential into a step function observed the appearance of band edges but did not reach the critical Fibonacci model[23]. Crucially, the IAAF (equation (2)) contains a constant energy shift, $\cos(\pi b)$, that guarantees the correct Fibonacci limit ($\beta \to \infty$). Accordingly, our IAAF model allows us to explore the emergence of criticality.

We first develop an intuitive picture of what we expect to observe: as β increases, the sampled function becomes steeper (Fig. 1a) and effectively should lead to stronger localization (that is, the region where the modes are extended shrinks) (Fig. 1b). More precisely, we theoretically investigate the transition to criticality by computing the eigenmodes of equation (1) and systematically analysing the

inverse participation ratio (IPR) of each eigenstate ψ_n as a measure of its localization:

$$\mathrm{IPR}_n \equiv \frac{\sum_{j=1}^{L} \left| \psi_{n,j} \right|^4}{\sum_{j=1}^{L} \left| \psi_{n,j} \right|^2} \tag{3}$$

where the sums run over length L of the chain. In the regime where the nth eigenmode ψ_n is extended, the IPR is equal to the inverse of the system length ($\mathrm{IPR}_n = 1/L$) and drops to 0 for an infinite system. Conversely, for modes localized on N sites, the IPR is equal to $1/N$ and remains finite for infinite system size.

In Fig. 1c–e, we summarize the IPR values obtained within the tight-binding analysis. Let us start with Fig. 1d, which illustrates the spectral dependence of the IPR for $\beta = 0$. The AA localization transition, occurring simultaneously for all eigenmodes at $\lambda/t = 2$, is clearly seen. Figure 1c shows the IPR of the lowest-energy eigenmode as a function of IAAF parameters λ/t and β. The IPR does not evolve monotonously with β but presents a cascade of lobes of higher IPR values (red regions, Fig. 1c) separated by minima of IPR (blue regions, Fig. 1c). Similar lobe structures occur for all eigenmodes (Supplementary Section III). At low λ/t, when increasing β, the region where all eigenmodes are extended decreases (green dashed line in Fig. 1c and Supplementary Section I). We now focus on the cascade to criticality for $\lambda/t = 5.5$, that is, starting from the strongly localized AA and continuously evolving toward the Fibonacci limit. As summarized in Fig. 1e, we observe that the lowest set of eigenmodes squeeze into a narrow spectral window, hybridize due to the finite hopping strength t, and delocalize at $\beta \approx 1.5$. We analytically obtain the position of the delocalization transition (Supplementary Section II), where, using Thouless's formula[24], we derive the condition for a diverging localization length for the lowest-energy
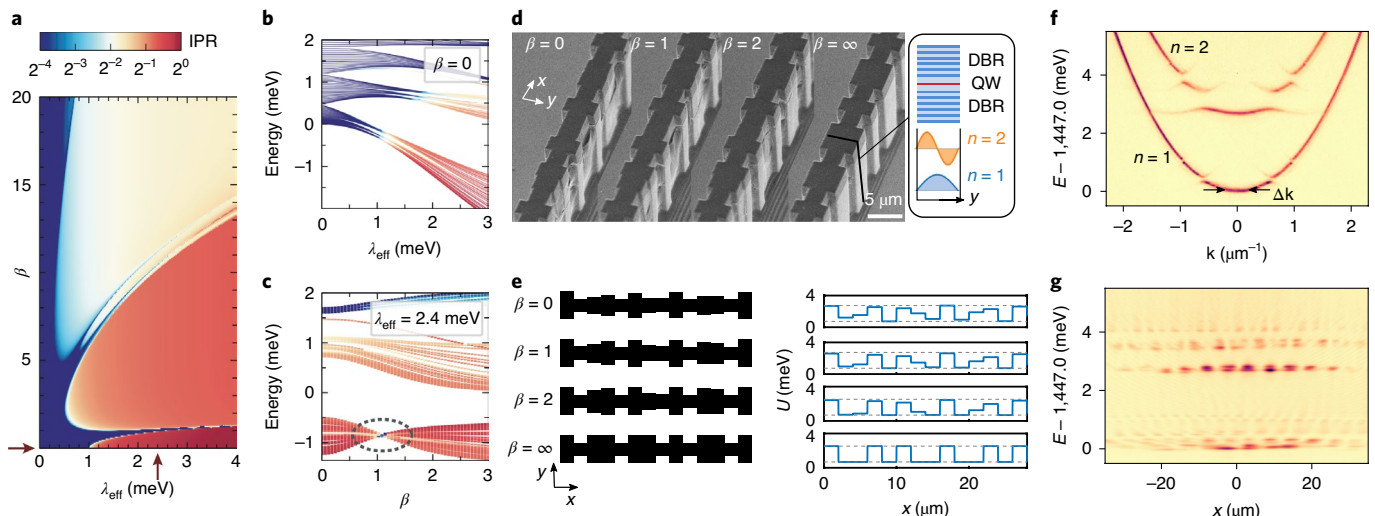
Fig. 2 | Continuum IAAF model and its experimental implementation. a, The IPR (see continuum version of equation (3) in Supplementary Section V) for the lowest-energy eigenmode of the continuum IAAF model (equation (4)). Two red arrows mark the constant β and λ_{eff} values used in **b** and **c**, respectively. **b**, The IPR of all eigenmodes of equation (4) as a function of energy and λ_{eff} for $\beta = 0$ (AA limit). **c**, The IPR of all eigenmodes of equation (4) as a function of energy and β for $\lambda_{\text{eff}} = 2.4$ meV. The region where the lowest band is delocalized is marked with a dashed oval. **d**, Scanning electron micrograph of four modulated polariton wires implementing the IAAF model for $\beta = 0$, 1, 2 and ∞. Inset: schematic representation (top) of the cavity structure along the z direction, with a single quantum well (QW) embedded between two distributed Bragg reflectors (DBRs). The transverse (y direction) profiles of the $n = 1$ and $n = 2$ polariton subbands are depicted below. **e**, Top views of the wire sections shown in **d** (left) and corresponding IAAF potential (right). **f**, Photoluminescence (PL) intensity measured as a function of momentum k and energy for a wire corresponding to $\beta = 0$ and $\lambda_1 = 0.2$ meV. The $n = 1$ and $n = 2$ sets of subbands are identified. **g**, PL intensity measured as a function of space x and energy for the same wire as in **f**.

eigenmode (dash-dotted line in Fig. 1c). By further increasing β, the modes localize once more with a smaller IPR. This process repeats at each minimum of the IPR (Fig. 1c). Furthermore, different bands exhibit this cascade at different values of β (Supplementary Section III). We conclude that the transition to criticality does not happen uniformly, but instead occurs through successive localization–delocalization transitions.

To observe experimentally these localization–delocalization transitions, we engineered cavity-polariton samples. This photonic platform has been used recently for the exploration of Fibonacci chains, whereby log-periodic oscillations of the density of states and a measure of topological invariants could be revealed by optical spectroscopy[25,26]. The quasiperiodic potential can be treated as a perturbation to the motion of free polaritons, namely, the Hamiltonian of this system can be written as a continuum model:

$$H\psi(x) = \left[-\frac{\hbar^2}{2m}\nabla^2 + \lambda_{\text{eff}} V(x, \beta) \right] \psi(x) \qquad (4)$$

where m is the polariton mass. The discrete modulation $V_j(\beta)$, given by equation (2), is implemented with a piecewise 1D potential $V(x, \beta) = V_{\lfloor x/a \rfloor}(\beta)$, with steps of length a. In Fig. 2a–c, we report the calculated IPR values obtained within the continuum IAAF model (equation (4)) (Supplementary Section V). For $\beta = 0$ (Fig. 2b), we observe signatures of the AA localization as a function of λ_{eff}. Note that, in contrast to the tight-binding model, the localization does not occur simultaneously for all modes, and mobility edges appear in the spectrum[27–30]. For the lowest band, the localization transition occurs at $\lambda_{\text{eff}} \approx 1$ meV, at approximately twice the relevant kinetic energy scale in the band (Supplementary Section VI). Importantly, as reported in Fig. 2a,c, the continuum model also exhibits the lobes of localization–delocalization transitions. Thus either of the two frameworks can be used for experiments.

We fabricated laterally modulated photonic wires based on polariton semiconductor microcavities. The sample was grown by molecular beam expitaxy to form a quantum well inserted between two high-reflectivity Bragg mirrors along the z direction (see Methods for further details). We processed the cavity sample into quasi-1D microstructures using electron-beam lithography and dry etching. The photonic modes (also called polaritons) form 1D-subbands with a distinct transverse spatial distribution (Fig. 2d). The lowest-energy subband ($n = 1$) presents modes with a maximum at the middle of the wire, while the $n = 2$ subband shows modes with intensity maxima left and right of the wire centre (Supplementary Section VII). For a given transverse mode n, the lateral confinement energy for polaritons is given by $U(w) = (\hbar^2\pi^2)/(2m) \times n^2/w^2$(ref. [25]), where w is the width of the wire. To implement the piecewise potential of the IAAF model (equation (4)), we consider etched sections (dubbed letters) of fixed length $a = 2$ μm and choose discrete values w_j of their width so that $U(w_j) = U_0 + \lambda_n V_j(\beta)$, where U_0 is a global offset determined by $U(\max(w_j))$. The scanning electron microscopy images in Fig. 2d show polariton structures implementing four values of β (top views are schematically represented in Fig. 2e, left). The corresponding potentials (Fig. 2d, right) present steps that progressively evolve into the two-valued Fibonacci sequence. Interestingly, due to the proportionality of $U(w)$ with n^2, the modulation amplitude λ_n for higher-energy subbands is increased by a factor n^2 with respect to the $n = 1$ subband. It is thus possible to access larger values of $\lambda_{\text{eff}} = n^2\lambda_1$ when considering higher-energy subbands.

To explore the localization properties of polariton modes in these IAAF chains, we optically excite single wires cooled to 4 K using a weak non-resonant continuous-wave laser. The excitation spot is elongated along the wires and we analyse the spectrally resolved photoluminescence (PL) signal either in real or in momentum space (see Methods for further details). In Fig. 2f,g, we show an example of such measurements for $\beta = 0$ and $\lambda_1 = 0.2$ meV. Polariton subbands corresponding to $n = 1$ and $n = 2$ are clearly resolved. The lateral modulation results in the opening of minigaps, which are four times larger for the $n = 2$ than for the $n = 1$ subbands, as expected.
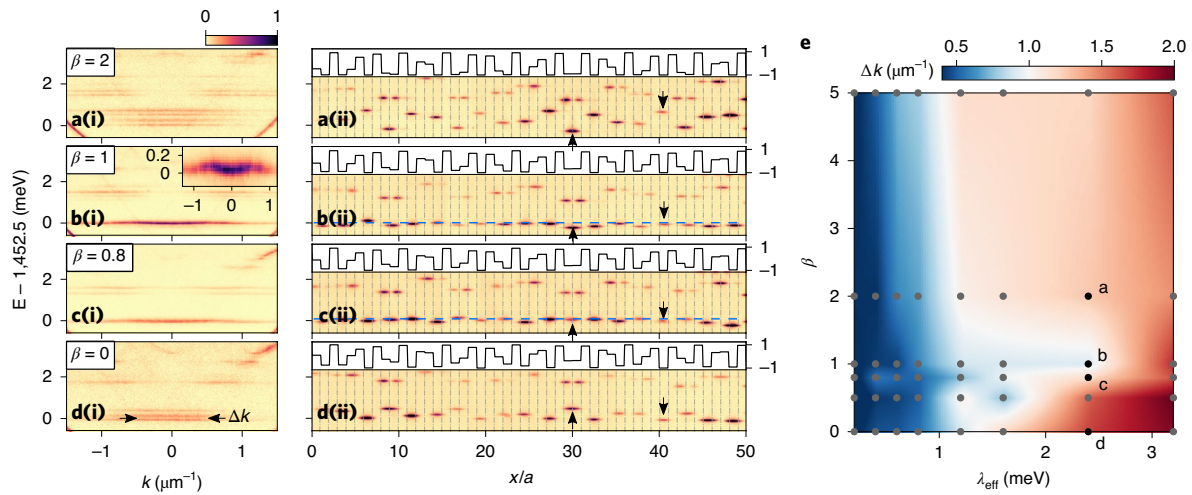
Fig. 3 | Experimental localization phase diagram. a(i)–**d**(i), PL intensity as a function of energy and k, zoomed on the $n = 2$ modes (Fig. 2f,g) for $\lambda_2 = 2.4$ meV and $\beta = 2$ (**a**(i)), $\beta = 1$ (**b**(i)), $\beta = 0.8$ (**c**(i)) and $\beta = 0$ (**d**(i)), as indicated in **e**. The inset in **b**(i) shows a magnified view of the lowest-energy band to highlight its curvature. **a**(ii)–**d**(ii), Corresponding real-space energy-resolved PL intensity. The vertical grey-dashed lines indicate the letter edges. On top of each panel, the nominal potential along the wire is depicted. The horizontal light blue dashed line marks the energy where the band hybridization takes place. Up (down) arrows mark the modes that invert their energies with β, which extend over two (one) letters. Modes localized on two letters have clear anti-bonding modes above them. **e**, Grey dots show FWHM Δk of the lowest-energy state (marked with arrows on **d**(i)) measured for several values of λ_{eff} and β. Colours are obtained by interpolation between measured points.

In the depicted example, all the polariton modes are extended in real space (Fig. 2g), indicating that this particular wire implements a metallic phase for the AA model.

Let us now discuss polariton localization properties when increasing the value of β. In Fig. 3a–d, we present PL measurements in real and reciprocal space for four values of β and constant λ_{eff}. For clarity, these figures only show the $n = 2$ subband that experiences $\lambda_2 = 2.4$ meV. For $\beta = 0$ (Fig. 3d), we observe localized emission spots in real space that are dispersed in energy. Accordingly, the emission is very broad in k-space. These features are characteristic of the AA localized phase. When β increases, we observe the merging of lowest-energy emission spots within a narrow spectral window. For $\beta = 1$, the k-space image reveals the formation of a band with a finite curvature (Supplementary Section VIII). This clearly indicates the formation of extended modes. By further increasing β, the polariton modes are localized once more. Thus, these measurements provide evidence for the first delocalization–localization transition when deforming the AA model into the Fibonacci chain. Every detail of the measured spatial patterns shown in Fig. 3a(ii)–d(ii) is reproduced by the continuum model simulations (Supplementary Section IX). Similar PL measurements were performed on different wires with various values of β and λ_{eff}. To quantify the polariton localization and obtain the phase diagram, we extract, from the measurements in k-space, the full-width at half-maximum (FWHM) Δk of the lowest-energy modes in the considered subband. Extended modes have lower Δk than localized ones. Figure 3e summarizes all the measured Δk values, clearly tracing the first delocalization lobe in the phase diagram, in agreement with theoretical predictions (Figs. 1c and 2a). In Supplementary Fig. 9 we show simulations of the polariton modes, both in real and reciprocal space, for higher values of β. The second delocalization transition is observed around $\beta = 10$. Such values of β were not present in the available sample. Nevertheless, simulations indicate the feasibility of experimentally observing the delocalization lobes at higher values of β.

Finally, we provide a physical understanding of the cascade of localization transitions discovered in the IAAF model. Careful analysis of the real-space PL images (Fig. 3a(ii)–d(ii)) reveals a key mechanism in the transition to criticality. In the AA limit

(Fig. 3d(ii)), we can see that all the lowest-energy modes are localized within one letter (for example, the downward-pointing arrow). Additionally, some modes, at higher energies, are localized on two sites corresponding to a two-letter potential minimum (for example, the upward-pointing arrow). These modes can be viewed as a bonding hybridization of two single-letter modes and are easily identified by the presence of a high-energy anti-bonding mode at the same spatial location. When increasing β, the potential of the two letters goes down towards the minimum of the Fibonacci potential and thus these two-letter bonding modes decrease in energy. They become resonant with the single-letter modes at the delocalization transition and then become the new lowest-energy state for larger β (arrows in Fig. 3a(ii)–d(ii)). Similarly, when considering the polariton modes across the second delocalization transition (see simulations in Supplementary Fig. 9), we see that the lowest-energy states evolve from two-letter to four-letter modes.

This spatial feature can be fully understood within the tight-binding approach. Starting at $\beta = 0$ (AA limit) and high λ, the spatial localization length of eigenmodes is known analytically to be $\xi = (\log \lambda / 2t)^{-1}$(refs. [5,6]). Thus, for $t \to 0$, all eigenmodes are expected to be localized on a single site. Nevertheless, the golden mean quasiperiodic modulation guarantees that pairs of modes always exist that are spatially nearest neighbours and close in energy (modes marked with a red dashed oval in Fig. 1a and nearly identical neighbouring two-letter potentials in Fig. 3a(ii)–d(ii)). These neighbouring modes hybridize with any finite hopping strength t, and are tuned with β to eventually overtake the role of the lowest-energy eigenmodes (Figs. 1c and 4, Supplementary Section IV and Supplementary Video 1). As a result the IPR is expected to be reduced by a factor of two across the transition.

Crucially, the mechanism of delocalization followed by relocalization repeats itself by further increasing $\beta \to \infty$. As seen in Fig. 4a, the IPR for both tight-binding (equation (1)) and continuum (equation (4)) models displays a series of plateaus whose heights decrease in a stepwise fashion. The former model exhibits steps that decrease by a factor of two every time a delocalization transition occurs. The latter shows deviations from this quantization due to the spatial extent of the continuum wavefunctions within a single letter
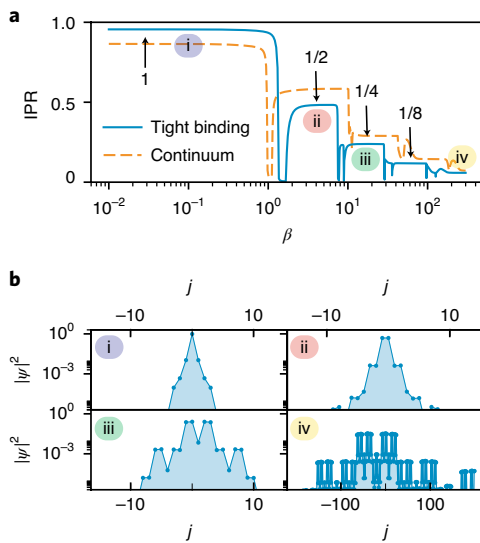
Fig. 4 | Spatial evolution with β of the lowest-energy eigenstate. a, The IPR (see equation (3) and its continuum version in Supplementary Section V) of the lowest-energy eigenmode as a function of β, calculated for $\lambda/t = 5.5$ (solid blue line) with the tight-binding model (equation (1)) and for $\lambda_{eff} = 2.4$ meV (dashed orange line) in the continuum model (equation (4)). The plateaux correspond to the localized regions of the phase diagram in Fig. 1c. **b**, Spatial profile of the lowest-energy eigenmode of the tight-binding model for $\lambda/t = 5.5$ and $\beta = \{0.01, 5, 15, 1,000\}$ (i, ii, iii, iv), respectively.

(see description of the continuum model IPR in Supplementary Section V). The spatial distribution of the localized eigenmodes on different plateaux is reported in Fig. 4b. We thus reveal that the transition to criticality at $\beta = \infty$, where the eigenmodes are self-similar, develops in the IAAF through a unique iterative process of eigenmodes hybridization that doubles the spatial extent of the eigenmodes (Supplementary Video 2).

To conclude, our work reports a new mechanism of the localization of waves in paradigmatic quasiperiodic models. These controlled band-selective localization–delocalization transitions provide a tunable knob by which to engineer selective bandpass filters. This approach opens up a new frontier where generalizations of the mechanism to other models, with different modulation frequencies and interpolations, can be addressed. Furthermore, the polaritonic platform uniquely promotes the study of quasiperiodic physics under the influence of non-Hermiticity and of nonlinearities on wave localization.

Online content

Any methods, additional references, Nature Research reporting summaries, source data, extended data, supplementary information, acknowledgements, peer review information; details of author contributions and competing interests; and statements of data and code availability are available at https://doi.org/10.1038/s41567-020-0908-7.

References

1. Anderson, P. W. Absence of diffusion in certain random lattices. *Phys. Rev.* **109**, 1492–1505 (1958).
2. Akkermans, E. & Montambaux, G. *Mesoscopic Physics of Electrons and Photons* (Cambridge Univ. Press, 2007).
3. Suck, J.-B., Schreiber, M. & Häussler, P. *Quasicrystals: An Introduction to Structure, Physical Properties and Applications* Vol. 55 (Springer, 2013).
4. Kraus, Y. E. & Zilberberg, O. Topological equivalence between the Fibonacci quasicrystal and the Harper model. *Phys. Rev. Lett.* **109**, 116404 (2012).
5. Aubry, S. & André, G. Analyticity breaking and Anderson localization in incommensurate lattices. *Ann. Israel Phys. Soc.* **3**, 133–140 (1980).
6. Jitomirskaya, S. Y. Metal–insulator transition for the almost Mathieu operator. *Ann. Math.* **150**, 1159–1175 (1999).
7. Kohmoto, M., Kadanoff, L. P. & Tang, C. Localization problem in one dimension: mapping and escape. *Phys. Rev. Lett.* **50**, 1870–1872 (1983).
8. Ostlund, S., Pandit, R., Rand, D., Schellnhuber, H. J. & Siggia, E. D. One-dimensional Schrödinger equation with an almost periodic potential. *Phys. Rev. Lett.* **50**, 1873–1876 (1983).
9. Lee, P. A. & Ramakrishnan, T. V. Disordered electronic systems. *Rev. Mod. Phys.* **57**, 287–337 (1985).
10. Evers, F. & Mirlin, A. D. Anderson transitions. *Rev. Mod. Phys.* **80**, 1355–1417 (2008).
11. Segev, M., Silberberg, Y. & Christodoulides, D. Anderson localization of light. *Nat. Photon.* **7**, 197–204 (2013).
12. Aulbach, C., Wobst, A., Ingold, G.-L., Hnggi, P. & Varga, I. Phase-space visualization of a metal–insulator transition. *New J. Phys.* **6**, 70 (2004).
13. Mastropietro, V. Localization of interacting fermions in the Aubry–André model. *Phys. Rev. Lett.* **115**, 180401 (2015).
14. Schreiber, M. et al. Observation of many-body localization of interacting fermions in a quasirandom optical lattice. *Science* **349**, 842–845 (2015).
15. Bordia, P., Lschen, H., Schneider, U., Knap, M. & Bloch, I. Periodically driving a many-body localized quantum system. *Nat. Phys.* **13**, 460–464 (2017).
16. Macé, N., Laorencie, N. & Alet, F. Many-body localization in a quasiperiodic Fibonacci chain. *SciPost Phys.* **6**, 050 (2019).
17. Varma, V. K. & Žnidarič, M. Diffusive transport in a quasiperiodic Fibonacci chain: absence of many-body localization at weak interactions. *Phys. Rev. B* **100**, 085105 (2019).
18. Verbin, M., Zilberberg, O., Kraus, Y. E., Lahini, Y. & Silberberg, Y. Observation of topological phase transitions in photonic quasicrystals. *Phys. Rev. Lett.* **110**, 076403 (2013).
19. Verbin, M., Zilberberg, O., Lahini, Y., Kraus, Y. E. & Silberberg, Y. Topological pumping over a photonic Fibonacci quasicrystal. *Phys. Rev. B* **91**, 064201 (2015).
20. Kraus, Y. E. & Zilberberg, O. Quasiperiodicity and topology transcend dimensions. *Nat. Phys.* **12**, 624–626 (2016).
21. Kraus, Y. E., Lahini, Y., Ringel, Z., Verbin, M. & Zilberberg, O. Topological states and adiabatic pumping in quasicrystals. *Phys. Rev. Lett.* **109**, 106402 (2012).
22. Harper, P. G. Single band motion of conduction electrons in a uniform magnetic field. *Proc. Phys. Soc. A* **68**, 874–878 (1955).
23. Hiramoto, H. & Kohmoto, M. New localization in a quasiperiodic system. *Phys. Rev. Lett.* **62**, 2714–2717 (1989).
24. Thouless, D. J. A relation between the density of states and range of localization for one dimensional random systems. *J. Phys. C* **5**, 77–81 (1972).
25. Tanese, D. et al. Fractal energy spectrum of a polariton gas in a Fibonacci quasiperiodic potential. *Phys. Rev. Lett.* **112**, 146404 (2014).
26. Baboux, F. et al. Measuring topological invariants from generalized edge states in polaritonic quasicrystals. *Phys. Rev. B* **95**, 161114 (2017).
27. Biddle, J., Priour, D. J., Wang, B. & Das Sarma, S. Localization in one-dimensional lattices with nonnearest-neighbor hopping: generalized Anderson and Aubry–André models. *Phys. Rev. B* **83**, 075105 (2011).
28. Ganeshan, S., Pixley, J. H. & Das Sarma, S. Nearest neighbor tight binding models with an exact mobility edge in one dimension. *Phys. Rev. Lett.* **114**, 146601 (2015).
29. Lüschen, H. P. et al. Single-particle mobility edge in a one-dimensional quasiperiodic optical lattice. *Phys. Rev. Lett.* **120**, 160404 (2018).
30. Roati, G. et al. Anderson localization of a non-interacting Bose–Einstein condensate. *Nature* **453**, 895–898 (2008).

Methods

Sample description. The quasiperiodic structures used in this work were etched out of a planar semiconductor microcavity with high quality factor ($Q \approx 75,000$), grown by molecular beam epitaxy. The microcavity consisted of a λ GaAs layer embedded between two $Ga_{0.9}Al_{0.1}As/Ga_{0.05}Al_{0.95}As$ DBRs with 36 (top) and 40 (bottom) pairs. A single 8 nm $In_{0.05}Ga_{0.95}As$ QW was inserted at the centre of the cavity, resulting in strong exciton–photon coupling, with an associated 3.5 meV Rabi splitting. After epitaxy, the sample was processed with electron-beam lithography and dry etching to form 1D wires with modulated width. The modulation consisted of sections of fixed length $a = 2\,\mu m$ and different width w_j, designed to implement the IAAF potential $U(w_j)$, with chosen (λ_1, β). The maximum section width was fixed to $4\,\mu m$, corresponding to the minimum of the effective 1D potential.

The exciton–photon detuning, defined as the energy difference between the uncoupled planar cavity mode and the exciton resonance, was of the order of $\delta = -20\,meV$ for all experiments.

Experimental technique. Non-resonant photoluminescence measurements were realized with a single-mode continuous-wave laser at 780 nm. The elongated spot was engineered using a cylindrical lens. Emission was collected through a microscope objective with $NA = 0.5$ and imaged on the entrance slit of a spectrometer coupled to a charge-coupled device camera with a spectral resolution of $\sim 30\,\mu eV$. Real- and momentum-space photoluminescence images were realized by imaging the sample surface and the Fourier plane of the objective, respectively. A polarizer was used to select emission polarized either along or across the long axis of the chains. The sample was cooled to $T = 4\,K$.

Data availability

Source data are available for this paper. All other data that support the plots within this paper and other findings of this study are available from the corresponding author upon reasonable request.

Author contributions

A.Š. and J.L.L. performed the tight-binding theoretical work. V.G. and N.P. developed the continuum model simulations. V.G. and C.D. designed the samples. A.L., L.L.G., A.H. and I.S. fabricated the samples. V.G., N.P. and C.D. performed the experiments. V.G., A.Š., N.P., J.L.L., S.R., A.A., J.B. and O.Z. contributed to the data analysis (simulations and experiments), scientific discussions and the writing of the manuscript. J.B. and O.Z. supervised the work.

Competing interests

The authors declare no competing interests.

Additional information

Supplementary information is available for this paper at https://doi.org/10.1038/s41567-020-0908-7.

Correspondence and requests for materials should be addressed to J.B. or O.Z.

Reprints and permissions information is available at www.nature.com/reprints.